



# Artificial formate oxidase reactivity with nano-palladium embedded in intrinsically microporous polyamine (Pd@PIM-EA-TB) driving the H<sub>2</sub>O<sub>2</sub> – 3,5,3',5'-tetramethylbenzidine (TMB) colour reaction



Lina Wang<sup>a</sup>, Mariolino Carta<sup>b</sup>, Richard Malpass-Evans<sup>c</sup>, Neil B. McKeown<sup>c</sup>, Philip J. Fletcher<sup>d</sup>, Pedro Estrela<sup>e,f</sup>, Alberto Roldan<sup>g,\*</sup>, Frank Marken<sup>a,f,\*</sup>

<sup>a</sup> Department of Chemistry, University of Bath, Claverton Down, Bath BA2 7AY, UK

<sup>b</sup> Department of Chemistry, Swansea University, College of Science, Grove Building, Singleton Park, Swansea SA2 8PP, UK

<sup>c</sup> EaStChem School of Chemistry, University of Edinburgh, Edinburgh EH9 3FJ, UK

<sup>d</sup> Materials & Chemical Characterisation Facility (MC<sup>2</sup>), University of Bath, Bath BA2 7AY, UK

<sup>e</sup> Department of Electronic & Electrical Engineering, University of Bath, Bath BA2 7AY, UK

<sup>f</sup> Centre for Biosensors, Bioelectronics and Biodevices (C3Bio), University of Bath, Bath BA2 7AY, UK

<sup>g</sup> Cardiff Catalysis Institute, School of Chemistry, Cardiff University, Main Building, Park Place, CF10 3AT Cardiff, UK

## ARTICLE INFO

### Article history:

Received 23 August 2022

Revised 20 October 2022

Accepted 8 November 2022

Available online 13 November 2022

### Keywords:

Clark probe

Disinfection

Oxidase

Cavity catalysis

Bipolar catalyst

Nanozyme

## ABSTRACT

Surface cavities formed by molecularly rigid polymers of intrinsic microporosity affect catalytic processes. Palladium nanoparticles of typically 3 nm diameter are formed in an intrinsically microporous polyamine (PIM-EA-TB) by borohydride reduction. These particles are shown to indirectly catalyse the oxidative colour change of indicator dye 3,5,3',5'-tetramethylbenzidine (TMB) in the presence of formic acid via formation of H<sub>2</sub>O<sub>2</sub>. Investigation reveals that oxygen reduction on the palladium is rate limiting with optimised H<sub>2</sub>O<sub>2</sub> production at approximately pH 3 to 4, and first order in formate, followed by purely homogeneous TMB oxidation. The H<sub>2</sub>O<sub>2</sub> production is therefore studied separately as a nanozyme-like catalytic process equivalent to formate oxidase reactivity, linked to the molecularly rigid polyamine host (PIM-EA-TB) providing ammonium sites (in molecularly rigid surface cavities) that enhance both (i) 2-electron formate oxidation and (ii) 2-electron oxygen reduction to H<sub>2</sub>O<sub>2</sub>. Beneficial effects of hydrophobic ClO<sub>4</sub><sup>-</sup> anions are noted as indirect evidence for the effect of ammonium sites in surface cavities. A computational DFT model for the artificial formate oxidase reactivity is developed to underpin and illustrate the hypothesis of PIM-EA-TB as an active catalyst component with implications for future nanozyme sensor development.

© 2022 The Author(s). Published by Elsevier Inc. This is an open access article under the CC BY license (<http://creativecommons.org/licenses/by/4.0/>).

## 1. Introduction

Mimicking enzyme processes is of considerable interest for example in electroanalysis [1,2] and in biosensing [3]. Formate oxidase enzyme reactivity is linked to the production of hydrogen peroxide, H<sub>2</sub>O<sub>2</sub>, via formate oxidation [4] (equation 1 and 2). The hydrogen carrying cofactor in formate oxidase is FAD/FADH<sub>2</sub>. Due to the significant range of applications of H<sub>2</sub>O<sub>2</sub>, this type and similar peroxide producing enzymes/nanozymes [5] are of considerable interest [6,7].



Formate oxidase reactivity towards formic acid in nature [8] has been discovered in aspergillus in 2009 as a FAD (chemically modified) cofactor dependent process [9]. It should be noted that there are also related more common enzymes such as formate dehydrogenase with NAD<sup>+</sup>/NADH cofactor [10]. The catalytic production of H<sub>2</sub>O<sub>2</sub> from formic acid has been exploited and suggested to be useful in a diverse range of synthetically relevant oxidation chemistries [11]. It is interesting to mimic the formate oxidase reactivity with chemically robust synthetic catalyst components. Here, the reactivity toward formic acid of palladium nanoparticles embedded into a polymer of intrinsic microporosity [12] host (PIM) is investigated.

Polymers of intrinsic microporosity (or PIMs [13]) are based on polymer materials with molecularly stiff backbone (see molecular

\* Corresponding authors.

E-mail address: [f.marken@bath.ac.uk](mailto:f.marken@bath.ac.uk) (F. Marken).

structure of PIM-EA-TB in Fig. 1B). The lack of polymer folding/packing causes poor interactions in the solid state and therefore (i) good processability and (ii) formation of highly porous materials (for PIM-EA-TB typically  $1000 \text{ m}^2\text{g}^{-1}$  surface area,  $1 \text{ cm}^3\text{g}^{-1}$  cumulative pore volume, and typically  $1 \text{ nm}$  micropore size when dry [14]). These rigid micropores are interesting in the context of catalysis due to the stiff molecular backbone creating “surface cavity” structures with effects on catalytic sites. Both molecular catalysts [15,16] and nanoparticulate catalysts [17,18] have been shown to retain activity when immobilised into the PIM host material. The molecularly rigid host has been proposed to embed the catalyst with only weak molecular interactions and without capping the active catalyst surface [19]. Here, palladium nanoparticles are embedded into PIM-EA-TB and investigated in aqueous formic acid containing solution. Screening of catalyst performance is based on catalyst-coated Clark probes (Fig. 1A), revealing both oxygen and hydrogen levels, and on  $\text{H}_2\text{O}_2$  detection.

Palladium nanoparticles are readily formed within microporous polyamines when adsorbed palladate  $\text{PdCl}_4^{2-}$  [20] is reduced with borohydride. In a recent report [21], it was shown that Pd@PIM-EA-TB was produced with typically  $3 \text{ nm}$  diameter palladium nanoparticles embedded into the polymer film. In the presence of formic acid, these nanoparticles form hydrogen peroxide (in the presence of low concentration of  $\text{HCOOH}$ ) and hydrogen (in the presence of higher concentrations of  $\text{HCOOH}$ ). The rate of  $\text{H}_2\text{O}_2$  production was reported to be sensitive to reaction conditions and to the presence of additional metals such as gold [22]. In fact, palladium-gold catalysts in the presence of  $\text{H}_2\text{O}_2$  have been shown to very reactive even towards inert molecules such as methane [23]. Here, the direct effects of the PIM-EA-TB host material on the catalytic reaction are investigated more closely. Nanozyme reactivity related to formate oxidase is suggested with the PIM-EA-TB creating catalytic cavities with palladium and taking an active role in the mechanism due to tertiary amine sites in proximity of the palladium surface.

Nanozymes [24,25] are non-biological catalysts that mimic biological reactivity and have attracted considerable attention for applications where biological enzymes (often less robust) can be replaced with an artificial catalyst with chemically robust properties. Nanozyme applications include electrochemical biosensors [26], in point-of-care diagnostics [27], in food safety [28], and in environmental analysis [29]. Nanozymes have been employed previously for the 3,5,3',5'-tetramethylbenzidine (TMB) colour reac-

tion [30]. Glucose oxidase mimicking nanozymes with TMB colour response have been reported [31,32]. Palladium nanoparticles have been reported as peroxidase mimics in TMB sensors for antioxidants in fruit juice [33].

In this report, the immobilisation and reactivity of a Pd(0) catalyst into the micropores of molecularly highly rigid host (PIM-EA-TB) is investigated. Based on Clark probe measurements and mass spectroscopy, it is shown that in a single process Pd@PIM-EA-TB catalysts react with formic acid and oxygen to give hydrogen peroxide. The combination of Pd nanoparticles and PIM-EA-TB is shown to operate most effectively in the pH range 3–4. A DFT model is employed to rationalise  $\text{H}_2\text{O}_2$  production processes within the Pd@PIM-EA-TB catalyst and to underpin the hypothesis of a direct role of PIM-EA-TB in the catalytic cycle. The hydrogen peroxide can then drive reactions such as the solution oxidation of 3,5,3',5'-tetramethylbenzidine (TMB) to give a blue colour response, which is useful for example in sensing. This process is optimised by dye accumulation into Nafion ionomer and could be of future interest in immuno-assays and colorimetric sensing.

## 2. Methodology

### 2.1. Reagents

$\text{PdCl}_2$  (99 %), HCl (ACS reagent, 37 %),  $\text{NaBH}_4$  (powder, 98 %),  $\text{HCOOH}$  (96 %, ACS Reagent), 3,3',5,5'-Tetramethylbenzidine (TMB,  $\geq 99\%$ ),  $\text{H}_3\text{PO}_4$  (85 wt% solution, ACS Reagent),  $\text{NaH}_2\text{PO}_4$  (99 %),  $\text{NaCOOH}$  (ACS reagent,  $\geq 99.0\%$ ), *p*-nitrophenylboronic acid ( $\geq 95.0\%$ ),  $\text{Na}_2\text{CO}_3$  (powder,  $\geq 99.5\%$ , ACS Reagent), and Whatman® nitrocellulose membrane filters (gridded white, pore size  $0.45 \mu\text{m}$ ) were products of Sigma-Aldrich. Acetic acid ( $\text{CH}_3\text{COOH}$ ,  $>99\%$ ) was the product of Fisher Scientific. Hydrogen peroxide ( $\text{H}_2\text{O}_2$ , ACS Reagent, 30 wt% in  $\text{H}_2\text{O}$ ) and dimethyl sulfoxide (DMSO, for HPLC,  $\geq 99.7\%$ ) were purchased from Honeywell.  $\text{NaHCO}_3$  ( $\geq 99.7\%$ ) was bought from Fluka. PIM-EA-TB was synthesised following the method of a previous paper [34]. Nylon mesh from  $75 \mu\text{m}$  diameter Nylon was purchased from Amazon.com (Therpin reusable Nylon fine mesh food strainer bag). A Fisherbrand universal indicator pH paper (pH 1–14) was used to roughly adjust the pH of test solution in the  $\text{H}_2\text{O}_2$  quantification procedure. Filter paper (Whatman™, pore size  $< 2 \mu\text{m}$ ) was ordered from GE Healthcare Life Sciences.

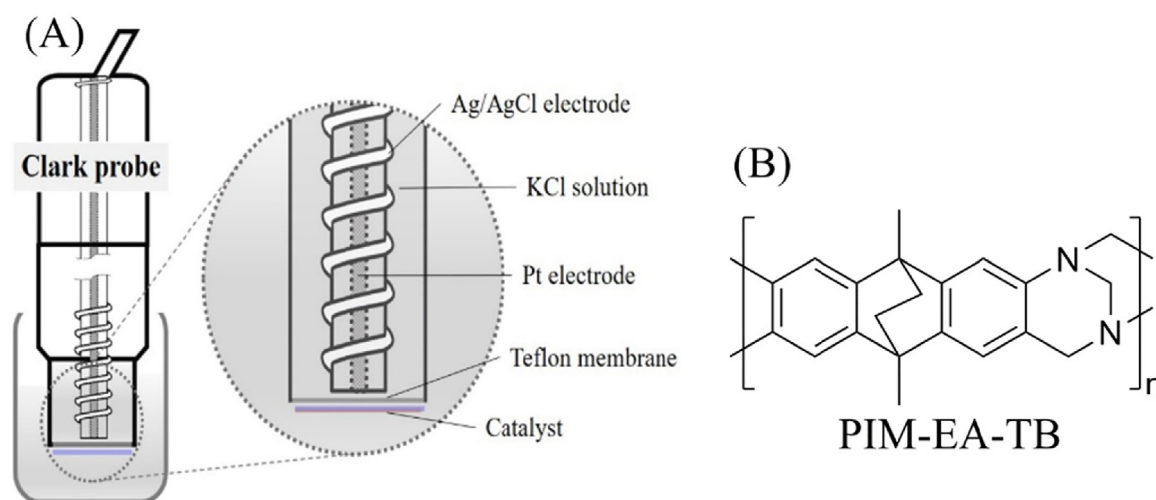


Fig. 1. (A) Schematic of a Clark probe for sensing oxygen or hydrogen. (B) Molecular structure for PIM-EA-TB.

## 2.2. Instrumentation

Ultra-pure water (resistivity not <math>18.2\text{ M}\Omega\text{ cm}</math> at  $20\text{ }^\circ\text{C}</math>) used in this work was purified by a Thermo Scientific water purification system. The pH of the buffer solution was measured by a pH meter (Jenway 3505). Clark probe (HI76407) and concentrated KCl solution (HI7041S) were purchased from HANNA Instruments Ltd., UK. Hydrogen production and oxygen consumption were monitored by chronoamperometry using a potentiostat (Metrohm  $\mu\text{Autolab II}$ ). To evaluate the morphology and elemental distribution of the product, a field emission scanning electron microscope (FESEM, JEOL JSM-7900F), a scanning electron microscope (SEM, Hitachi SU3900) and an attached energy dispersive X-ray analyser ( $170\text{ mm}^2$  Ultim Max EDX) were applied. More information about particle size and distribution of Pd particles were obtained from a transmission electron microscope (TEM, JEOL JEM-2100PLUS). A liquid chromatography-mass spectroscopy (LC-MS) technique with an Agilent 6545 Accurate-Mass Q-TOF LC/MS system was used for the quantification measurement of the  $\text{H}_2\text{O}_2$  product.$

## 2.3. Procedures

**Nylon disk substrates for catalysts.** Commercial Nylon mesh ( $75\text{ }\mu\text{m}$  threads, woven, with approx.  $130\text{ }\mu\text{m} \times 130\text{ }\mu\text{m}$  open holes; approx.  $200\text{ }\mu\text{m}$  pitch cheesecloth bag for straining almond/soy milk, XelNaga, Amazon.com) was cut into round disks with  $8\text{ mm}$  diameter as the substrate for catalyst deposits. Then,  $20\text{ }\mu\text{g}$  of PIM-EA-TB ( $1\text{ mg/mL}$  in chloroform) was drop-cast on both sides of the Nylon disk. After chloroform evaporation, the disk with PIM-EA-TB coating was immersed in  $5\text{ mg/mL}$   $\text{PdCl}_2$  in  $1\text{ M}$  HCl solution for  $1\text{ h}$ . Under these conditions predominantly  $\text{PdCl}_4^{2-}$  is formed [35]. A visible colour change to orange occurs due to  $\text{PdCl}_4^{2-}$  binding. Then the disk was rinsed with water and placed into aqueous  $\text{NaBH}_4$  solution ( $5\text{ mg/mL}$ , freshly made) for  $20\text{ h}$  in a refrigerator at  $4\text{ }^\circ\text{C}$ . A dark product containing Pd nanoparticles

immobilised into PIM-EA-TB was formed as illustrated in Fig. 2A. Fig. 2B shows the SEM and corresponding EDX elemental mapping for the product of Pd@PIM-EA-TB on the Nylon mesh. The PIM-EA-TB appears to coat uniformly on the Nylon mesh as evidenced by nitrogen elemental distribution consistent with the position of Nylon. The distribution of Pd reveals where the PIM-EA-TB is located, suggesting uniformly distributed particles embedded in PIM-EA-TB. The morphology of the film is characterised by FESEM as shown in Fig. 2C. The film-like deposit is composed of some small particles with sizes of typically tens of nanometers probably caused by aggregation of polymer during deposition.

In order to investigate Pd nanoparticles within PIM-EA-TB, samples were ultrasonicated in isopropanol to separate the Pd@PIM-EA-TB polymer film from the Nylon substrate. The TEM images in Fig. 3 indicate that Pd nanoparticles with mean particle size of  $3.0 \pm 0.1\text{ nm}$  are formed embedded in the microporous PIM-EA-TB film.

**Hydrogen peroxide detection.** Hydrogen peroxide quantification was carried out following a previously reported method [21]. Briefly,  $\text{H}_2\text{O}_2$  reacts with *p*-nitrophenol boronic acid stoichiometrically in alkaline conditions and produces *p*-nitrophenol. The amount of *p*-nitrophenol is then detected and analysed using a LC-MS system (Agilent 6545 Accurate-Mass Q-TOF LC/MS system). Thus, with a calibration curve the concentration of  $\text{H}_2\text{O}_2$  is obtained.

**Colorimetric assay based on TMB.** All colorimetric experiments related to TMB were carried out in the dark and at room temperature. The reagents (TMB, formic acid, sodium formate, hydrochloric acid, perchloric acid, catalyst on Nylon mesh substrate, etc.) were placed into a glass vial (typically  $10\text{ mM}$  HCOOH, pH 3.75,  $580\text{ }\mu\text{M}$  TMB, 33% DMSO, with a solution volume of  $11\text{ mL}$  in total). Colour changes in the vials were monitored/recorded photographically over time.

The TMB colour response was amplified by accumulation onto a strip of filter paper ( $7 \times 1.8\text{ cm}^2$ ) by stamping

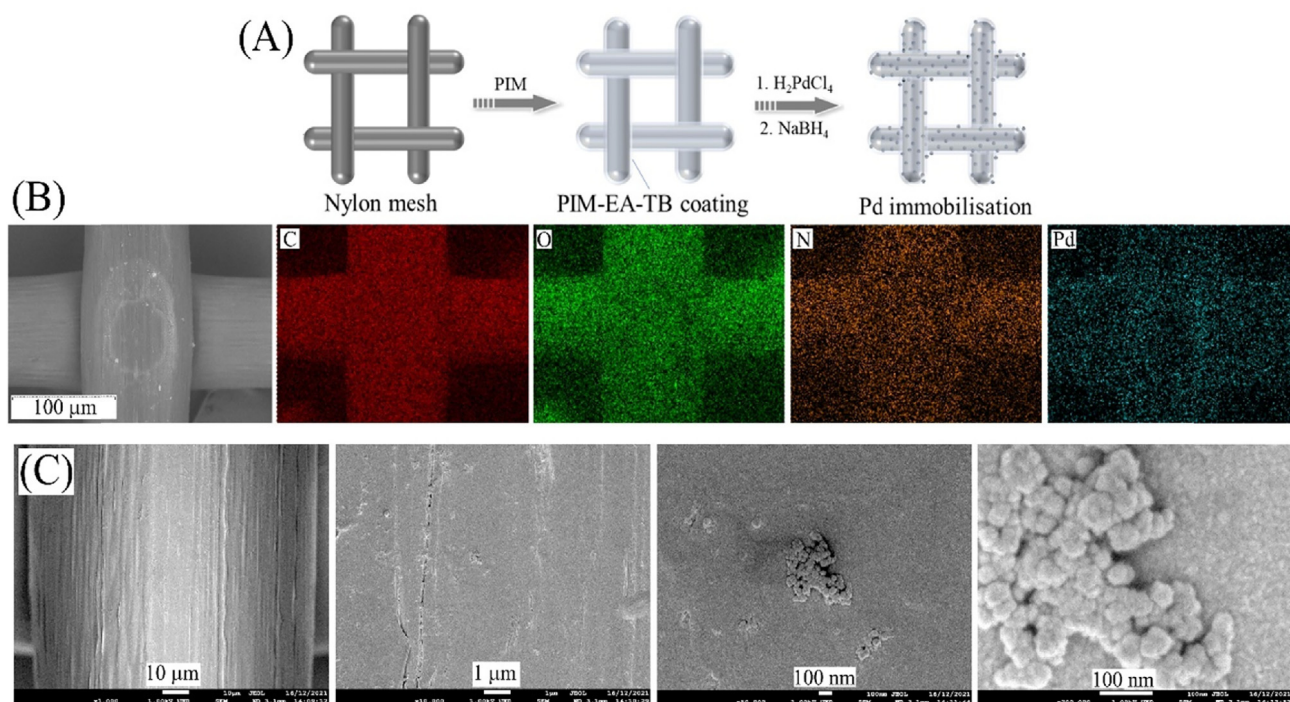


**Fig. 2.** (A) Illustration of the Nylon impregnation with PIM-EA-TB followed by binding of  $\text{PdCl}_4^{2-}$  and borohydride reduction. (B) Scanning electron microscopy image (back scatter mode) and EDX mapping for C, O, N, and Pd. (C) Field emission scanning electron microscopy (FESEM) images of the Pd@PIM-EA-TB coated Nylon fibre with  $5\text{ nm}$  sputter coated chromium to suppress charging.

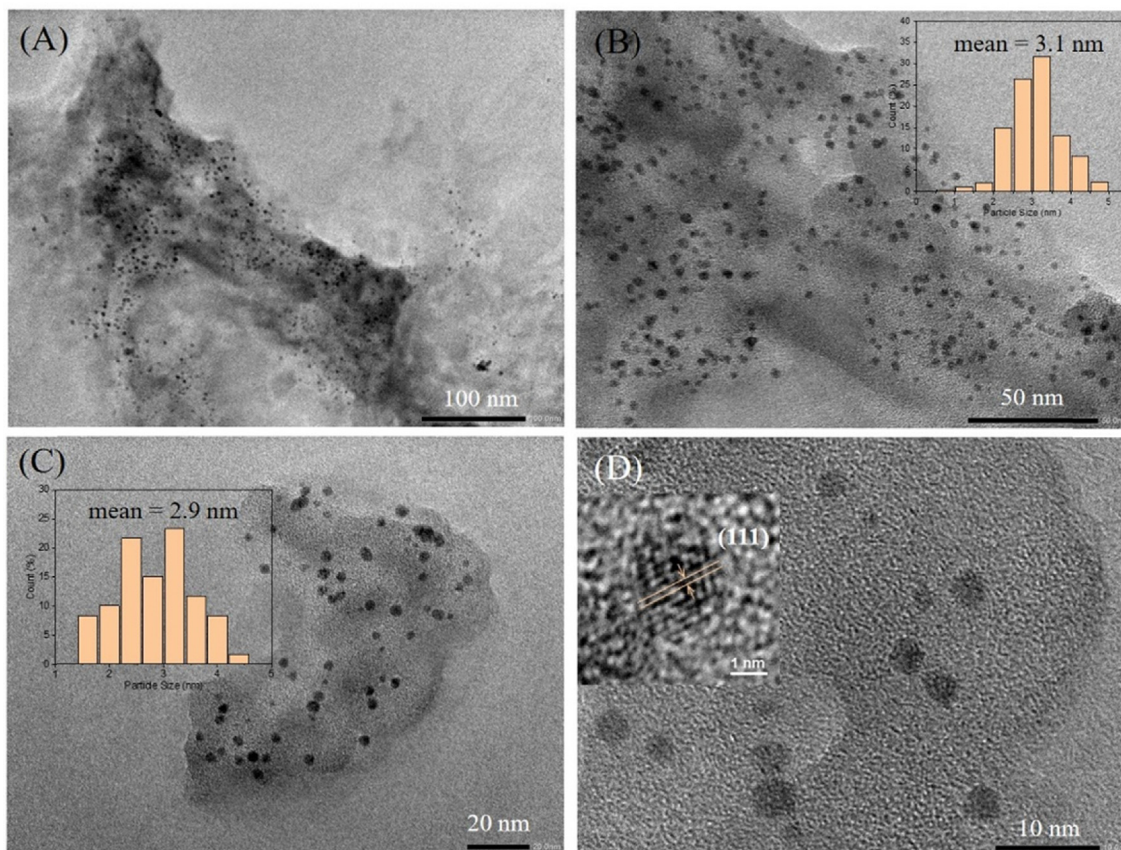


**Fig. 3.** Transmission electron microscopy (TEM) images for Pd@PIM-EA-TB. (A) Pd nanoparticles distributed in PIM-EA-TB. (B, C) Higher magnification images show particles with mean size of  $3.0 \pm 0.1$  nm (insets: size distribution of Pd nanoparticles). (D) High-resolution image showing d-spacing of 0.22 nm indicating the (111) crystal facet of Pd.

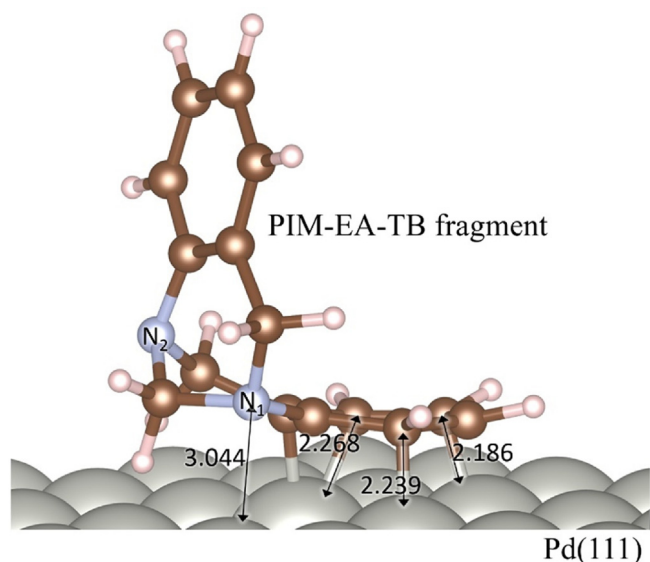


**Fig. 4.** Schematic representation of the PIM-EA-TB fragment on its most favourable adsorption configuration on a  $p(5 \times 5)$  Pd(111) supercell. Distances are given in Å. Grey, brown, pale blue and white balls indicate Pd, C, N and H atoms respectively. (For interpretation of the references to colour in this figure legend, the reader is referred to the web version of this article.)

(<https://www.getstamped.co.uk>) a solution of 100  $\mu$ L solution mixture of 80 wt% Nafion (5 % solution, Sigma-Aldrich) and 20 wt% 1-butanol (ACS reagent,  $\geq 99.4$  %, Sigma-Aldrich).

**Computational Details.** We have carried out spin-polarised density functional theory (DFT) calculations using the Vienna Ab initio Software Package (VASP [36]) to investigate the HCOOH decomposition and  $\text{H}_2\text{O}_2$  formation on Pd particles in presence and absence of PIM-EA-TB. The method offers a good compromise between accurate physical model and computational costs: the model considers the most stable palladium surface, Pd(111), and an active PIM-EA-TB fragment based on a monomeric unit. The exchange–correlation contributions were calculated using the generalized gradient approximation (GGA) with the revised functional of Perdew–Burke–Ernzerhof (RPBE [37]). The core electrons were described using the Projected Augmented Wave (PAW) formalism [38], and a kinetic energy cutoff of 450 eV was chosen for the valence electron plane-wave basis set. The Brillouin zone was sampled with a  $k$ -spacing of  $0.2 \text{ \AA}^{-1}$ . The convergence criteria were set to  $-0.03 \text{ eV \AA}^{-1}$  for the ionic and  $10^{-5} \text{ eV}$  for the electronic threshold. The zero-damping Grimme’s empirical correction (D3) accounted for the long-range dispersion interactions [39]. Appropriate dipole corrections were used perpendicular to the surfaces upon molecular adsorptions. The solvent effect of water was calculated by an implicit polarised continuum model (PCM), which describes the interaction between a solvent and solute in plane-wave DFT [40,41] without adding explicit water molecules to the model.

The Pd surface is represented by a slab model with a thickness of 5 atomic layers, the bottom 3 layers frozen at the optimised solid lattice and the top 2 layers free to relax in any direction. The dimension of the supercell is of  $p(3 \times 3)$  for bare Pd and  $p(5 \times 5)$  for the adsorbed PIM-EA-TB fragment. A vacuum of 15 Å perpendicular to the surface was added to eliminate the interaction between

periodic images. The PIM-EA-TB fragment was placed with the ring parallel and perpendicular to the surface. The ring parallel to the Pd (111) results in an interaction 0.61 eV more stable than the ring perpendicular (see Figure S1). Isolated molecules were placed in an asymmetric simulation cell large enough to avoid any spurious interaction with periodic images. The adsorption energies ( $E_{\text{ads}}$ ) were calculated using equation 3, where  $E_{\text{system}}$  is the energy of the adsorbate on the slab,  $E_{\text{slab}}$  and  $E_{\text{molecule}}$  are the energy of the clean surface (without PIM-EA-TB) and the energy of the isolated adsorbate.

$$E_{\text{ads}} = E_{\text{system}} - (E_{\text{slab}} + E_{\text{molecule}}) \quad (3)$$

The reaction energy of each reaction step ( $E_{\text{R}}$ ) is given by the difference between the final and the initial state energies. We combined the climbing-image nudged elastic band (CI – NEB [42,43]) and the improved dimer method to find the saddle points of the transition states (TS) structures, linking the minima across the reaction profile [44]. All states have been characterized using vibrational analysis and confirmed that only TS have a single imaginary frequency. We defined the activation barrier ( $E_{\text{A}}$ ) as the energy difference between the initial and the transition state energies. All energies reported are corrected with the vibrational contribution at zero Kelvin, *i.e.*, the zero-point energy.

### 3. Results and discussion

#### 3.1. Pd@PIM-EA-TB reactivity I: Colorimetric evidence for $\text{H}_2\text{O}_2$ production from formic acid and oxygen

Colorimetric assays based on 3,5,3',5'-tetramethylbenzidine (TMB) reactivity towards  $\text{H}_2\text{O}_2$  are commonly employed in sensor systems [45]. Josephy *et al.* have reported aspects of the fundamental mechanism to explain the reactivity of TMB [46]. Based on this work, TMB reactivity and colour responses can be summarised in a reaction scheme [47] (Fig. 5A) based on two sequential one-electron oxidation processes. Colourless TMB is oxidised to the  $\text{TMB}^{+\bullet}$  radical, which is suggested to dimerise (with loss of a proton) into a blue charge transfer complex. The second oxidation leads to a yellow product (the diimine), which is often employed to quantify the reaction (*e.g.*, quantifying the presence of  $\text{H}_2\text{O}_2$ ) after addition of acidic stop solution. A green coloration is

commonly observed when both the charge transfer complex and the diimine are present.

Fig. 5B shows the time dependent development of colour for TMB in the presence of 0 mM to 100 mM formic acid. A Nylon disk with Pd@PIM-EA-TB catalyst was present during this reaction. A colour response is indicative for  $\text{H}_2\text{O}_2$  production at the Pd catalyst. Both the formic acid concentration and the pH could affect these processes. A strong colour response is observed at approx. 10 mM formic acid concentration. The function of the Pd catalyst may be associated with several of the reaction steps. The peroxidase activity of Pd [48] or other catalyst materials [49] catalysing the reaction of TMB with  $\text{H}_2\text{O}_2$  has been well documented. However, the molecular size of TMB is considerable (relative to the other reagents and relative to the micropore size in PIM-EA-TB) and therefore in this case permeation TMB or reaction intermediates/products into the micropores of the microporous PIM-EA-TB may be extremely slow or impossible. In fact, here the Pd catalysis for TMB oxidation can be ruled out (*vide infra*).

Next, in order to explore pH effects, a solution of 10 mM formate/formic acid is employed and only the pH is varied (Fig. 6A). A pattern emerges where pH 3 or pH 3.5 give significant colour responses. Therefore, both the pH and the formate/formic acid concentration affect the overall reaction. A mildly acidic pH value between 3 and 4 appears to be most effective (although the reasons for this need further exploration).

There are several possible reasons for these effects and the reaction needs to be dissected and studied in two separate stages (Fig. 6C): (**Process I**) the production of  $\text{H}_2\text{O}_2$  and (**Process II**) the oxidation of TMB in the presence of  $\text{H}_2\text{O}_2$ . Fig. 6B shows that there is considerable reactivity for TMB and  $\text{H}_2\text{O}_2$  in 10 mM formic acid as well as in 10 mM acetic acid in the absence of Pd@PIM-EA-TB (possibly involving peroxyformate or peroxyacetate). Peroxyformic acid has been employed in the past in lignin bleaching and delignification processes [50] as well as for epoxidation of natural oils [51,52]. Peroxyformic acid for epoxidation reactions is formed when combining formic acid and hydrogen peroxide in an equilibrium [53,54]. Similar reactivity in perchloric, hydrochloric, or phosphoric acid is less obvious, although phosphoric acid at pH 4.5 ( $\text{NaH}_2\text{PO}_4$ ) also triggers a weak TMB colour change (Fig. 6B). The mechanistic details for this TMB oxidation in the absence of intentionally added catalyst are currently not clear, but this result

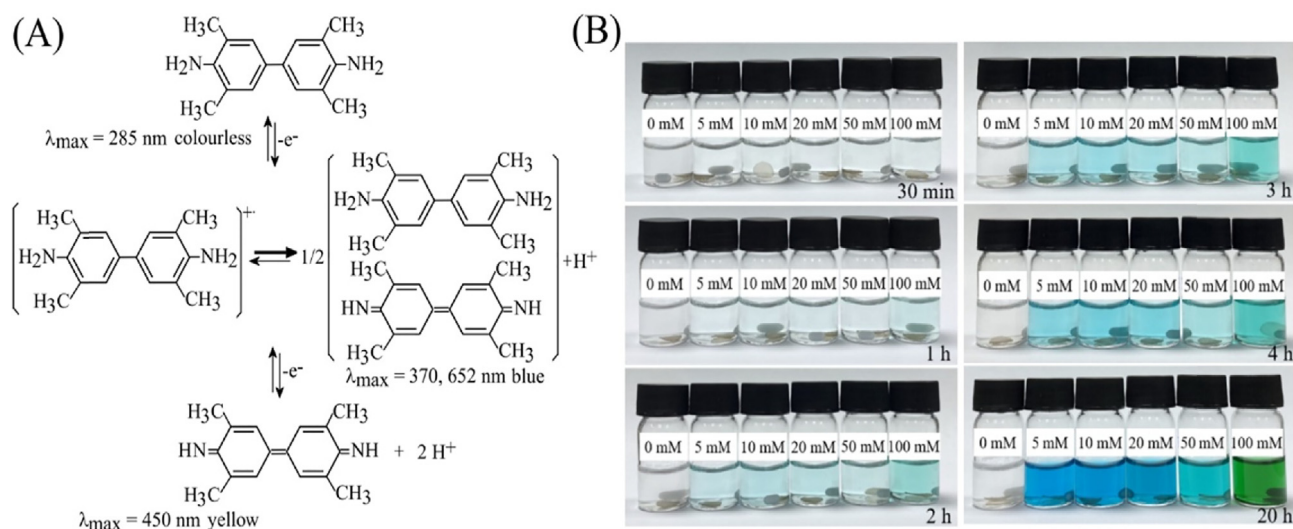


**Fig. 5.** (A) Reaction scheme for the TMB colour reaction induced by oxidation [29]. (B) Effect of concentration of formic acid on TMB reactivity in the presence of Pd@PIM-EA-TB. Photographs are shown of vials with 580  $\mu\text{M}$  TMB in different concentration of formic acid ranging from 0 to 100 mM (stirred in the dark, 16% DMSO to aid solubility) as a function of reaction time.

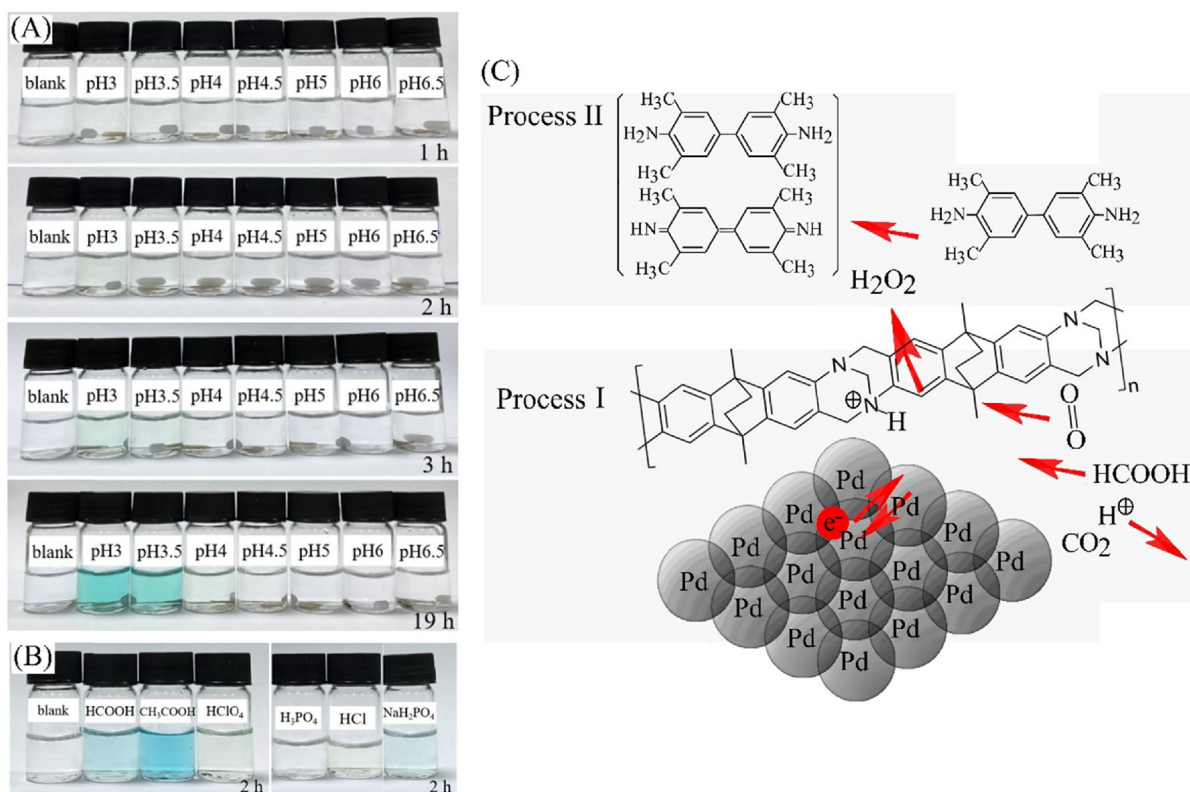


**Fig. 6.** (A) Effect of pH values on TMB reactivity. Photographs of 580 μM TMB in 10 mM HCOOH/HCOONa with a pH value ranging from 3 to 6.5 in the presence of Pd@PIM-EA-TB (stirred in the dark, 16 % DMSO) as a function of reaction time. (B) Effect of acids on H<sub>2</sub>O<sub>2</sub> catalysis for TMB. Photographs of 580 μM TMB in 10 mM H<sub>2</sub>O<sub>2</sub> in the presence of 10 mM formic, acetic, perchloric, phosphoric, hydrochloric acid, and for 10 mM NaH<sub>2</sub>PO<sub>4</sub> (reaction time 2 h, no catalyst, 16 % DMSO to aid solubility). (C) Illustration of the TMB oxidation process in the presence of Pd@PIM-EA-TB and HCOOH: Pd catalysed formation of H<sub>2</sub>O<sub>2</sub> (Process I) followed by homogeneous oxidation of TMB (Process II). Illustration of Pd atoms not to scale.

suggests that TMB does not have to permeate through micropores to interact with the Pd@PIM-EA-TB catalyst in order to produce a colour reaction. The molecular structure of TMB (Fig. 6C) would suggest a considerable size and therefore very slow transport (if any) in the micropores of the polymer of intrinsic microporosity. **Process II** is therefore considered to be essentially homogeneous and separate from **Process I**, which requires the catalysis at Pd@PIM-EA-TB. Next, **Process I** and the formate oxidase reactivity of Pd@PIM-EA-TB are further investigated in the absence of TMB.

### 3.2. Pd@PIM-EA-TB reactivity II: Formate oxidase reactivity

Fig. 7A shows that the production of H<sub>2</sub>O<sub>2</sub> with Pd@PIM-EA-TB in aqueous 20 mM formic acid is effective and essentially constant

over 3 h reaction time (with stirring). When exploring the effect of formic acid concentration (at 2 h reaction time; see Fig. 7B) a “switch-on” effect is noted close to 10 mM HCOOH with the H<sub>2</sub>O<sub>2</sub> production rate approaching a plateau at higher formic acid concentrations. This plateau in H<sub>2</sub>O<sub>2</sub> production could be linked to a kinetic limit (Michaelis-Menten effects or a micropore mass transport effect) for the process in Pd@PIM-EA-TB, or it could be linked to the pH in the solution phase (which is more likely, *vide infra*). Data in Fig. 7C are obtained at constant pH of 3.75 and with varying formate/formic acid concentration. Clearly, the hydrogen peroxide production process is first order in formate/formic acid and not limited at fixed pH. Therefore, the plateau in data in Fig. 7B must be linked to the pH rather than to reagent binding or transport. This could be linked, for example, to the protonation

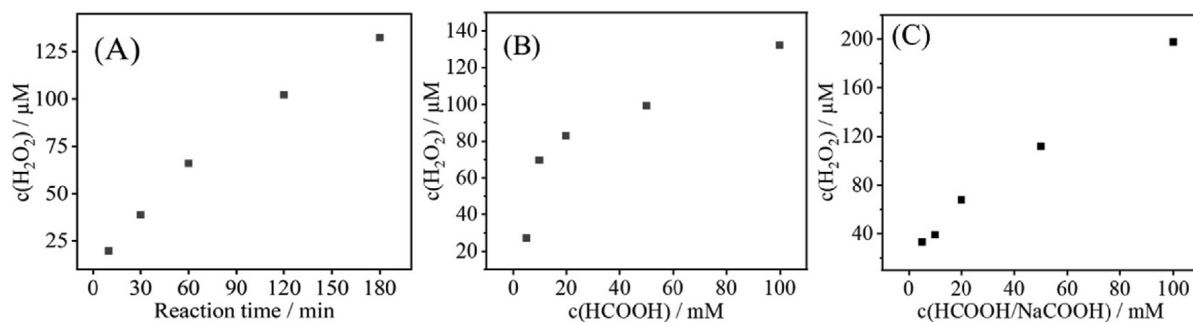


**Fig. 7.** (A) Plot of H<sub>2</sub>O<sub>2</sub> concentration as a function of time (one Nylon disk modified with Pd@PIM-EA-TB in 10 mL stirred solution) for 20 mM formic acid concentration. (B) Plot of H<sub>2</sub>O<sub>2</sub> concentration after 2 h reaction (one Nylon disk modified with Pd@PIM-EA-TB in 2 mL stirred solution) as a function of formic acid concentration. (C) Plot of H<sub>2</sub>O<sub>2</sub> concentration after 2 h reaction (one Nylon disk modified with Pd@PIM-EA-TB in 2 mL stirred solution) as a function of formic acid concentration at fixed pH of 3.75.

of PIM-EA-TB (with  $pK_A \approx 4$  [14]) switching on the enhanced catalytic process.

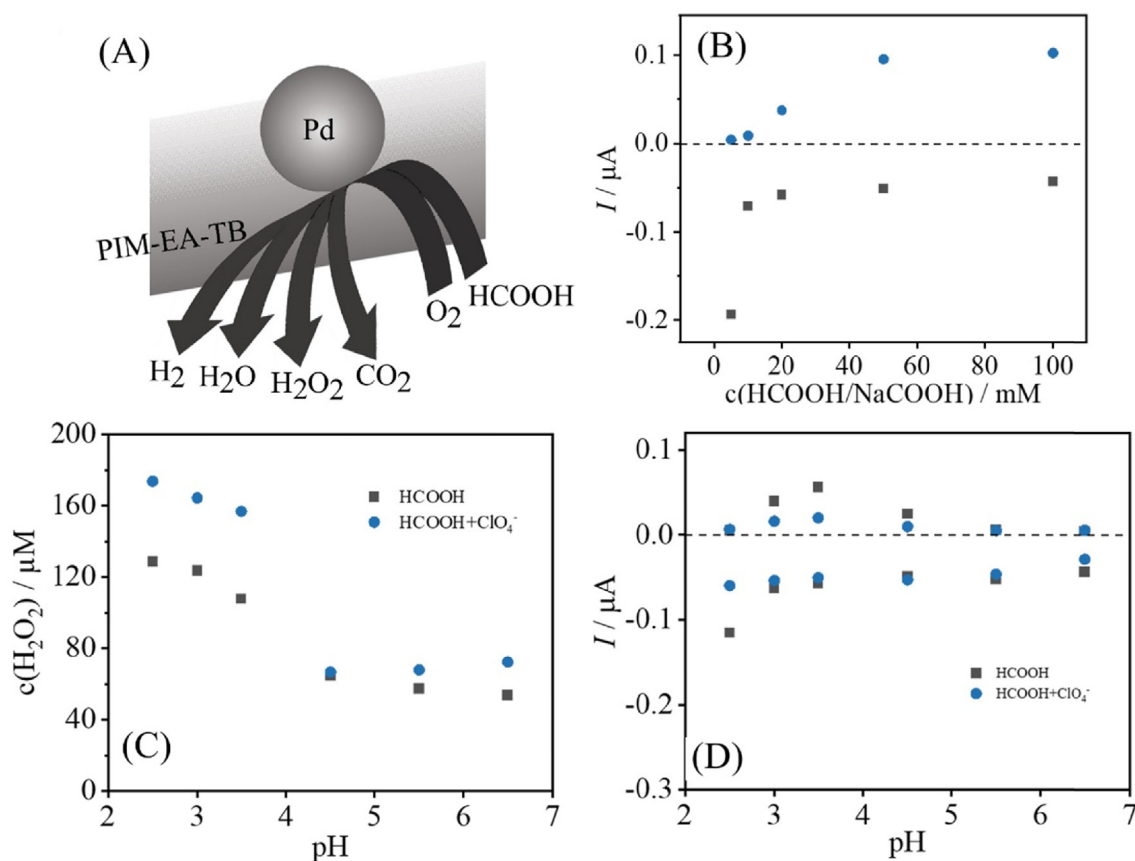
These data suggest that the formate/formic acid concentration is key to driving the  $H_2O_2$  production, but only if the pH is in the right range (between pH 3 and pH 4). This pattern of reactivity could be reflected also in other types of processes at the confined palladium catalyst particles. Important pH-dependent reactions here are (i) the consumption of  $O_2$ , (ii) the production of  $H_2O_2$ , (iii) the production of  $H_2O$ , and (iv) the production of  $H_2$  and  $CO_2$  from  $HCOOH$  (see Fig. 8A). Both oxygen consumption and hydrogen production can be conveniently monitored with Clark probe measurements [18]. Fig. 1A shows an illustration of the Clark probe with the catalyst (immobilised on a Nylon disk substrate) attached to the Teflon membrane outer surface. An applied potential of  $-0.7$  V vs Ag/AgCl allows oxygen detection and an applied potential of  $+0.6$  V vs Ag/AgCl allows hydrogen detection [21].

Fig. 8B shows combined data for oxygen consumption (negative current data) and for the production of hydrogen (positive current data). With a constant pH of 3.75, there is a transition at a concentration of approx. 10 mM formate/formic acid for both oxygen consumption (a plateau reading is observed at higher concentrations) and for hydrogen production (hydrogen production increases). In view of these data, it seems likely that a balance exists of  $H_2O_2$ ,  $H_2O$ , and  $H_2$  production. Oxygen is not fully consumed by the embedded catalyst, but hydrogen production is observed. In contrast to the conditions for catalysis in stirred solution (with the Nylon substrate floating in solution), at a Clark probe the solution is stagnant and locally mass transport of oxygen is therefore

slower. As a result, hydrogen production is more likely at the Clark probe and less likely in the stirred reaction. In the stirred catalyst solution,  $H_2O_2$  production should ultimately cease at higher formate/formic acid concentration but due to stirring this may only happen beyond the range shown in Fig. 7C (100 mM).

Further data from Clark probe experiments are shown in Fig. 8D. The pH is varied with a constant formate/formic acid concentration of 50 mM. The consumption of oxygen appears relatively constant over the pH range 2.5 – 6.5. However, the production of hydrogen peaks between pH 3 and pH 4. Therefore, making the solution more acidic will enhance hydrogen production, but, beyond pH 3, the presence of acid has a detrimental effect on hydrogen production. These phenomena are complex but could be connected to the presence of the PIM-EA-TB as a confined reaction space around the Pd nanoparticle catalyst (*vide infra*). The reduction of oxygen could be beneficially affected by protonation of PIM-EA-TB (providing a catalytic reaction site in the vicinity of the proton). In contrast, the reaction of formic acid might require the amine binding site in PIM-EA-TB (to receive a proton during hydrogen and carbon dioxide production). The binding ability of PIM-EA-TB towards protons and/or formic acid can be affected by additional anionic species such as hydrophobic perchlorate anions. Therefore, perchlorate is employed here to probe catalytic “cavity effects” in the PIM-EA-TB.

The effects of perchlorate are investigated as a probe for the effects of the PIM-EA-TB protonation on the catalytic formate oxidase reactivity. Perchlorate anions are known to be readily incorporated into PIM-EA-TB when the protonation of tertiary amine



**Fig. 8.** (A) Schematic reactions at Pd nanoparticles. (B) Effect of concentration of HCOOH at a fixed pH 3.5 on  $H_2$  and  $O_2$  levels. Plot of approximate Clark probe  $H_2$  response (blue) and  $O_2$  consumption response (black) versus formic acid concentration at pH of 3.75. (C) Plot of  $H_2O_2$  concentration formed at Pd@PIM-EA-TB in the presence of 50 mM HCOOH (or HCOONa) with/without 50 mM  $HClO_4$  (or  $NaClO_4$ ) as a function of pH. Data sets for 2 mL stirred solution without  $ClO_4^-$  (black), with  $ClO_4^-$  (blue) after 2 h reaction time. (D) Plot of Clark probe  $H_2$  and  $O_2$  responses in the presence of 50 mM HCOOH (or HCOONa) with (blue) or without (black) 50 mM  $ClO_4^-$  as a function of pH. (For interpretation of the references to colour in this figure legend, the reader is referred to the web version of this article.)

**Table 1**

DFT data for activation ( $E_A$ ) and reaction ( $E_R$ ) energies for the  $H_2O_2$  formation on PIM-EA-TB fragment/Pd(111) and on pristine Pd(111). Note that “\*” indicates bound species.

	PIM <sub>f</sub> /Pd(111)		Pd(111)	
	$E_A$ /eV	$E_R$ /eV	$E_A$ /eV	$E_R$ /eV
$O_2(g) \rightarrow O_2^*$	–	–0.80	–	–0.56
$O_2^* + H^* \rightarrow HOO^*$	0.15	–0.09	0.66	–0.26
$HOO^* \rightarrow HOOH^*$	0.11	0.04	0.75	–0.11
$HOOH^* \rightarrow H_2O_2(g)$	–	+0.72	–	+0.35

sites occurs [55]. Therefore, it is anticipated that perchlorate will enhance protonation of the amine sites as well as suppressing the binding of formic acid. When investigating the effect of pH on  $H_2O_2$  production with 50 mM formate/formic acid and 50 mM perchlorate, no difference is seen in the pH range > 4 (Fig. 8C). Only at pH 4 and below a significant increase in  $H_2O_2$  production with perchlorate is noticed. Protonation of PIM-EA-TB will occur at pH < 4, and the presence of  $ClO_4^-$  anions seems to affect the production of  $H_2O_2$  beneficially. It can be suggested (tentatively) that the presence of  $ClO_4^-$  anions will lead to a higher population of protonated tertiary amines without coordination of  $HCOO^-$ . This could lead to two effects: (i) the positive charge on the protonated amine can assist in the reduction of oxygen and (ii) the absence of the bound formate can lower the production of hydrogen. Both effects are seen in data in Fig. 8C and 8D. A comparison of reactivity of only PIM-EA-TB on Nylon, of Pd@PIM-EA-TB, of Pd nanoparticles extracted from Pd@PIM-EA-TB, and of a Pd film (25 mm thick, 5 mm × 5 mm area) is shown in Figure S2 demonstrating that Pd@PIM-EA-TB at pH 3.75 is the most effective catalyst. In addition, the effect of pH on  $H_2O_2$  production offers further direct supporting evidence for the beneficial effect of the host polymer on the reaction.

When investigating the consumption of oxygen and the production of hydrogen with a Clark probe (Fig. 8D), the addition of  $ClO_4^-$  clearly leads to a suppression of the hydrogen production in the pH range from 3 to 4. This can be considered as evidence for the effect of the protonated amine sites in PIM-EA-TB contributing to the catalytic mechanism, but experimentally the conditions within the microporous catalyst are difficult to explore. Therefore, we employed a DFT “cavity model” analysis to better envisage and understand reactions during hydrogen peroxide and hydrogen production in the Pd@PIM-EA-TB nanozyme cavity.

**Table 2**

Summary of DFT data for activation ( $E_A$ ) and reaction ( $E_R$ ) energies for the HCOOH decomposition on PIM-EA-TB fragment/Pd(111) and on pristine Pd(111). The ‡ superscript is employed to indicate that the H transferred to the Pd(111) surface or the PIM-N<sub>1</sub>. Note that “\*” indicates bound species.

	PIM-EA-TB fragment/Pd(111)		Pd(111)	
	$E_A$ /eV	$E_R$ /eV	$E_A$ /eV	$E_R$ /eV
$HCOOH(g) \rightarrow HCOOH^*$	–	–0.35	–	–0.41
$HCOOH^* \rightarrow HCOO^* + H^{\ddagger}$	0.02	–0.52	0.23	–0.11
$HCOO^* \rightarrow CO_2^* + H^{\ddagger}$	0.42	–0.65	0.75	–0.45
$HCOO^* \rightarrow HCO^* + O^*$	1.65	+0.79	1.67	+1.05
$HCOOH^* \rightarrow COOH^* + H^{\ddagger}$	0.76	–0.44	0.61	–0.25
$COOH^* \rightarrow CO_2^* + H^{\ddagger}$	0.19	–0.15	0.73	+0.02
$COOH^* \rightarrow CO^* + OH^*$	0.88	–0.25	0.83	–0.26

### 3.3. Pd@PIM-EA-TB reactivity III.: Nanozyme cavity effects probed by DFT

We carried out a computational mechanistic investigation at the PIM-EA-TB/Pd(111) interface to reveal further kinetic aspects for the hydrogen peroxide production upon dehydrogenation of formate/formic acid. The DFT approach is performed at high level with consideration of solvation effects. However, approximations are required for example when choosing the palladium metal surface sites, by selecting the polymer fragment, and by working at absolute zero temperature. Nevertheless, the DFT calculations are important as a tool to assess reaction path energetics and for future prediction of polymer cavity systems in catalytic reactions. For the calculation, a PIM-EA-TB fragment (Fig. 4) was selected. Among the various PIM-EA-TB fragment - Pd(111) interactions explored here, the structure depicted in Fig. 4 is the most stable, with an adsorption energy of –2.09 eV in the  $p(5 \times 5)$  supercell. Both nitrogen atoms in the PIM-EA-TB fragment structure can be protonated. However, N<sub>1</sub> (in Fig. 4) has a hydrogenation/protonation energy of –0.51 eV, 0.16 eV more favourable than on the N<sub>2</sub> site (note that in the DFT model, protonation is equivalent to hydrogenation with the electron going into the conduction band). In fact, the formation of N<sub>1</sub>H<sup>+</sup> is as favourable as hydrogenating the pristine Pd(111) surface ( $E_{ads} = -0.51$  eV). Therefore, we considered N<sub>1</sub> as the active amine group for both, the catalytic O<sub>2</sub> hydrogenation reaction and the catalytic HCOOH dehydrogenation reaction.

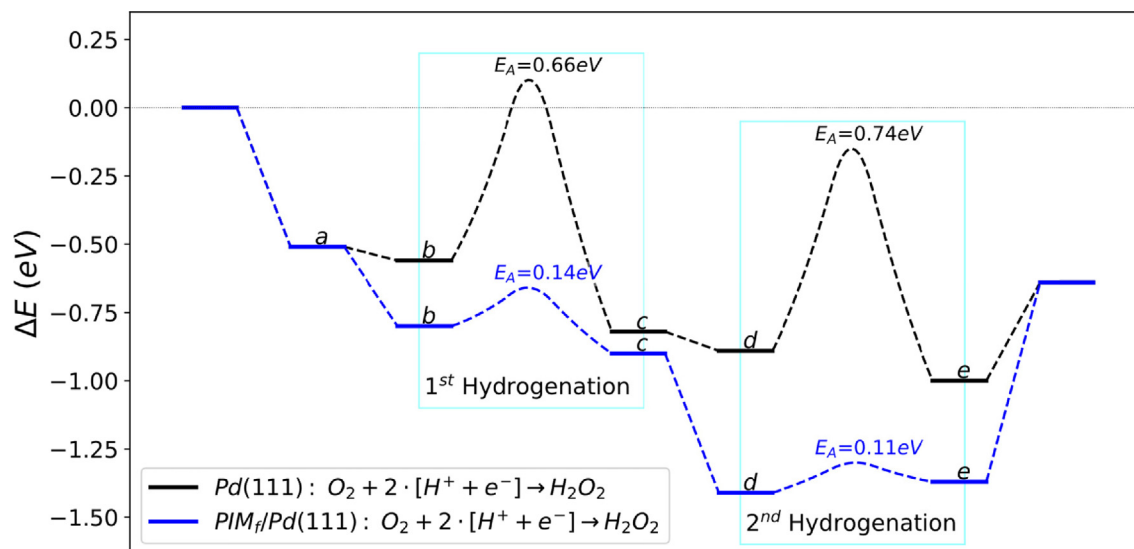


**Fig. 9.** Energy profile for the formation of  $H_2O_2$  from  $O_2$  on pristine Pd(111) and on PIM-EA-TB fragment/Pd(111). Inset values indicate the activation energies ( $E_A$ ) of elementary steps. Letters a–e represents the surface intermediates as depicted in Figure S3. The last step indicates the  $H_2O_2$  energy in the gas phase relative to reactants.

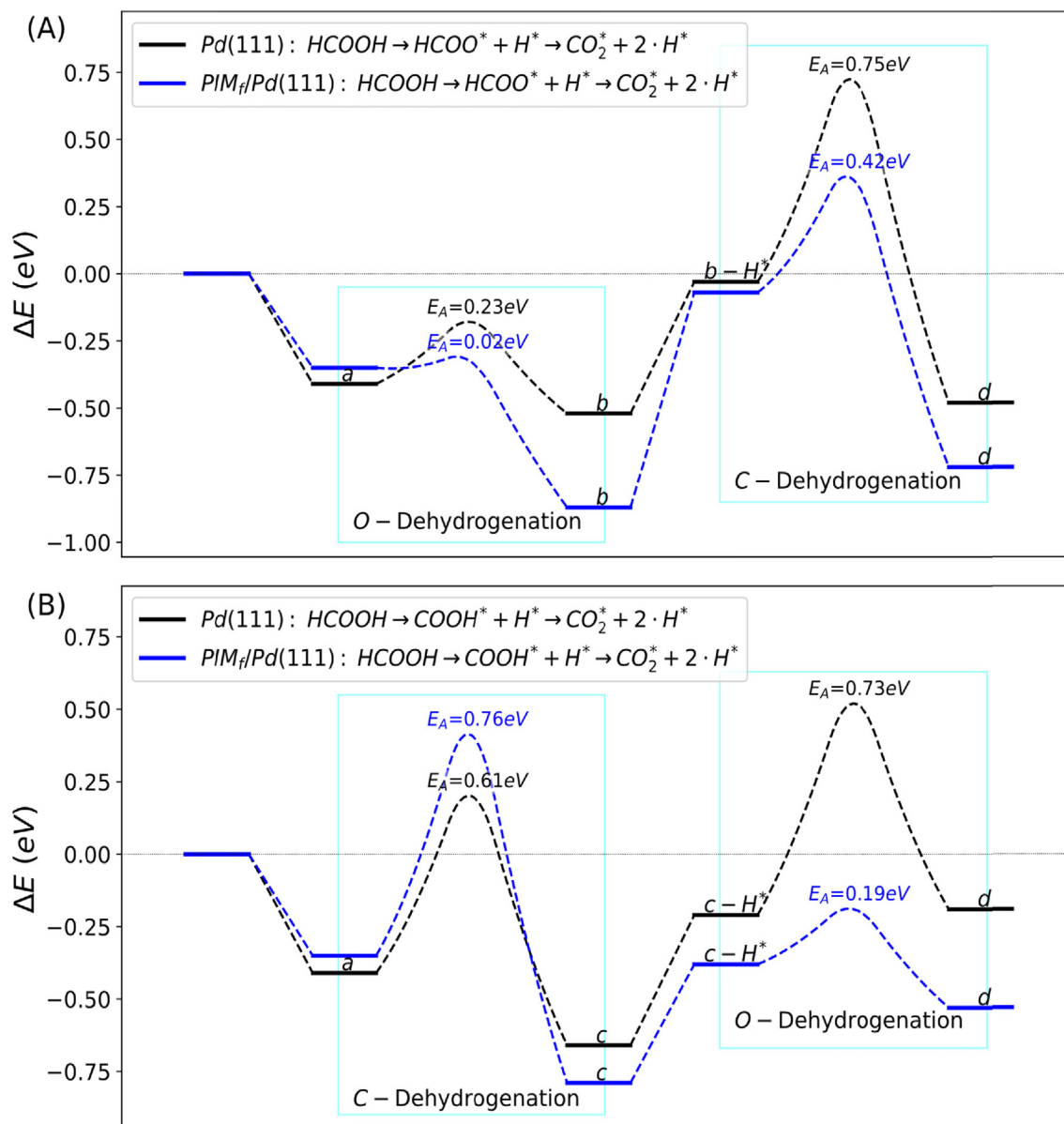


**Fig. 10.** Energy profiles for HCOOH decomposition to  $\text{CO}_2^*$  and  $2 \cdot \text{H}^*$  on pristine Pd(111) and on PIM-EA-TB fragment/Pd(111). (A) Energy profiles for C–H dehydrogenation followed by O–H dehydrogenation. (B) Energy profiles for O–H dehydrogenation followed by C–H dehydrogenation. Inset values indicate the activation energies ( $E_A$ ) of elementary steps. Letter **a–d** represents the surface intermediates as depicted in Figure S4. Also compare Figure S5. Note that “\*” indicates bound species.

**Oxygen Reduction to  $\text{H}_2\text{O}_2$ .** Starting from the protonated amine site in the PIM-EA-TB fragment (Fig. S3a), we simulated the co-adsorption of molecular oxygen on the Pd(111) surface. The molecular oxygen adsorption is energetically favourable ( $E_{\text{ads}} = -0.67 \text{ eV}$ ) and becomes more exothermic as the  $\text{O}_2$  approaches to the protonated  $\text{N}_1$  ( $E_{\text{ads}} = -0.80 \text{ eV}$  at  $2.637 \text{ \AA}$  from  $\text{N}_1\text{H}$ ; Fig. S3b). The O–O stretching mode ( $\nu_{\text{O-O}}$ ) changes from  $1563.4 \text{ cm}^{-1}$  in the gas phase to  $918.9 \text{ cm}^{-1}$  when  $\text{O}_2$  is co-adsorbed but still at  $3.061 \text{ \AA}$  from  $\text{N}_1\text{H}$ . The  $\nu_{\text{O-O}}$  vibration shifts to  $865.9 \text{ cm}^{-1}$  in intermediate **b**. Upon overtaking an activation energy of  $0.15 \text{ eV}$ , the first hydrogenation of molecular oxygen (Fig. S3c) takes place ( $E_{\text{R}} = -0.09 \text{ eV}$ ) decreasing even further  $\nu_{\text{O-O}}$  to  $532.5 \text{ cm}^{-1}$ . The slightly acidic solution ( $3 < \text{pH} < 4$ ) regenerates  $\text{N}_1\text{H}$  (Fig. S3d) and a slightly endothermic second hydrogenation forms  $\text{H}_2\text{O}_2$  after overcoming an activation energy of  $0.11 \text{ eV}$ . Adsorbed  $\text{H}_2\text{O}_2$  (Fig. S3e) presents a stretching frequency of  $718.1 \text{ cm}^{-1}$  and is located at  $-1.37 \text{ eV}$  below the energy reference, i.e., PIM-EA-TB fragment, molecular hydrogen, and molecular oxygen.  $\text{H}_2\text{O}_2$  requires  $+0.72 \text{ eV}$  to desorb

from the PIM-EA-TB fragment/Pd(111) surface. The gas phase  $\text{H}_2\text{O}_2$  presents an O–O distance of  $1.492 \text{ \AA}$  with O–O stretching of  $890.6 \text{ cm}^{-1}$ , which compare very well with the benchmark ( $1.475 \text{ \AA}$  and  $877 \text{ cm}^{-1}$ ) [56,57].

With the aim to highlight the importance of PIM-EA-TB in the catalytic process, we calculated the  $\text{H}_2\text{O}_2$  formation on pristine Pd(111) using the same computational approach. The results obtained are in good agreement with previous computational studies, considering the differences in functional and long-range energy contributions. [58] Table 1 summarises the energies along the reaction pathway, Fig. 9 summarises the energy profile of the  $\text{O}_2$  adsorption and hydrogenation to form  $\text{H}_2\text{O}_2$ , and the optimised structures on pristine Pd(111) are depicted in Figure S3 including insets of the key interatomic distances and angles.

The presence of PIM-EA-TB on the Pd surface significantly stabilises the co-adsorption of molecular oxygen (**b**), the HOO intermediates (**c** and **d**), and  $\text{H}_2\text{O}_2$  (**e**) leading to lower hydrogenation energy barriers compared to those on pristine Pd(111) by  $> 0.5 \text{ eV}$ . These

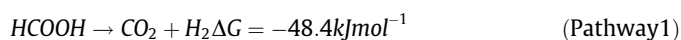


**Fig. 11.** (A) Effect of HCOOH/HCOONa concentration at pH 3.75 on TMB reactivity. Photographs of 580  $\mu\text{M}$  TMB the absence of Pd@PIM-EA-TB (stirred in the dark, 33 % DMSO) as a function of reaction time.  $\text{H}_2\text{O}_2$  was added to reflect reactivity as in data presented in Fig. 7C: blank: no  $\text{H}_2\text{O}_2$ , 5 mM: 33  $\mu\text{M}$ , 10 mM: 41  $\mu\text{M}$ , 20 mM: 59  $\mu\text{M}$ , 50 mM: 111  $\mu\text{M}$ , 100 mM: 198  $\mu\text{M}$   $\text{H}_2\text{O}_2$ . (B) Photographs of 580  $\mu\text{M}$  TMB the presence of Pd@PIM-EA-TB (stirred in the dark, 33 % DMSO) as a function of reaction time.  $\text{H}_2\text{O}_2$  was generated *in situ*.

results suggest that the dispersion of Pd(111) catalyst in the micro-porous structure of PIM-EA-TB is very likely to promote the formation of hydrogen peroxide. The cavity formed by PIM-EA-TB on the palladium surface is likely to enhance reaction rates. Note that we have not calculated side reactions for the  $\text{H}_2\text{O}_2$  decomposition which may also be affected by the presence of PIM-EA-TB.

**Formic Acid Dehydrogenation to  $\text{CO}_2$ .** To further define the role of PIM-EA-TB on formic acid decomposition, DFT calculations

were performed in which the protonation of  $\text{N}_1$  in the PIM-EA-TB fragment structure occurs. We carried out a mechanistic investigation on the HCOOH dehydrogenation process on palladium assessing the effects of PIM-EA-TB. It has been reported previously that the HCOOH decomposition on palladium may take different pathways forming either  $\text{CO}_2$  (Pathway 1) or CO (Pathway 2) [59–62].



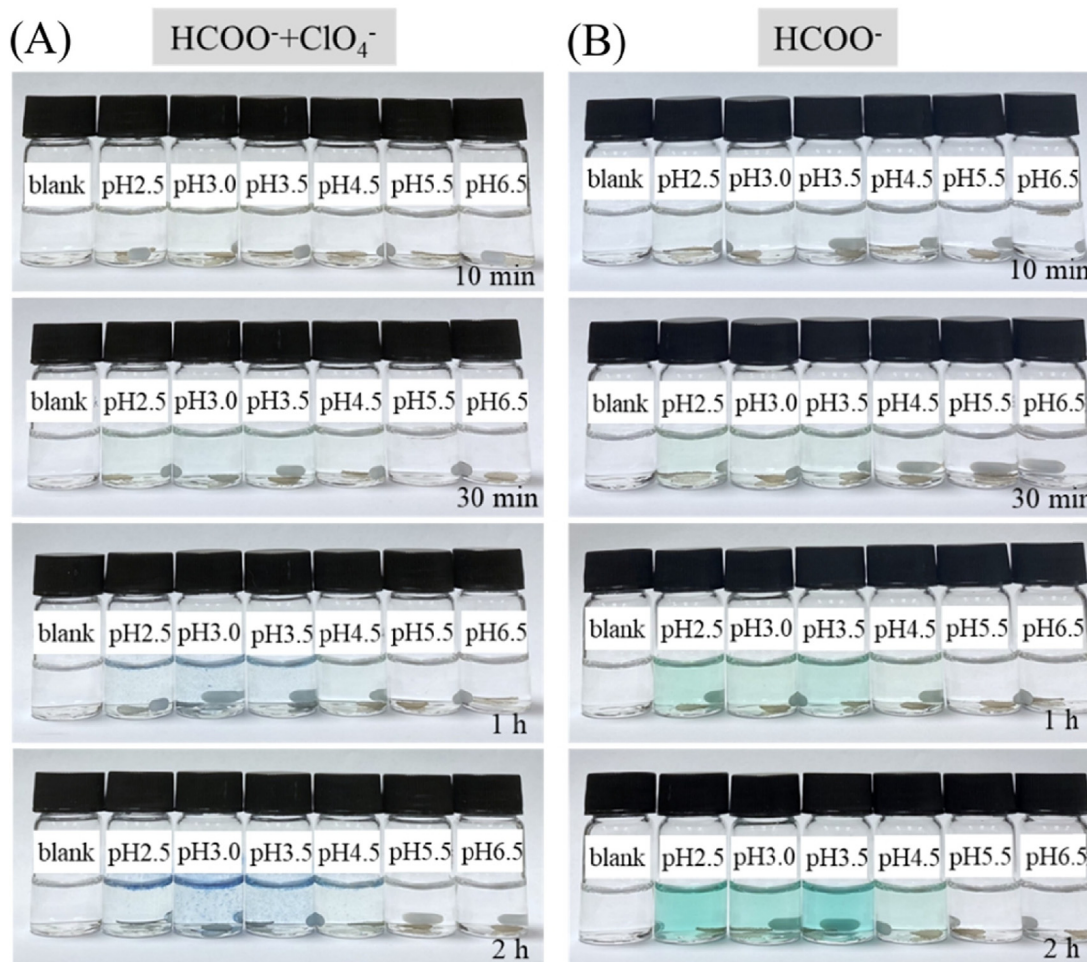


**Fig. 12.** Effect of 50 mM  $\text{ClO}_4^-$  for 50 mM  $\text{HCOOH}/\text{HCOONa}$  concentration at pH 3.75 on TMB reactivity. Photographs of 580  $\mu\text{M}$  TMB (A) in the presence and (B) in the absence of  $\text{ClO}_4^-$  with Pd@PIM-EA-TB (stirred in the dark, 33 % DMSO) as a function of reaction time.



Although the behaviour of formic acid molecules is dependent on the solution pH, we started the molecular decomposition on Pd(111) in its acid form ( $\text{HCOOH}$ , Fig. S4a). The molecule transfers exothermically its acidic proton to either the naked surface ( $E_R = -0.11$  eV) or preferably to the amine group in the co-adsorbed PIM-EA-TB fragment ( $E_R = -0.52$  eV) leaving formate ( $\text{HCOO}^*$ ) on the palladium surface (Fig. S4b). In addition to the  $\text{HCOO}^*$  decomposition, we also explore the formation and decomposition of the carboxylic surface species ( $\text{COOH}^*$ ; Fig. S4c) showing exothermic formation energy. Activation and reaction energies are summarised in Table 2 and an atomistic representation including key distances is provided in Figure S4.

The decomposition of  $\text{HCOO}^*$  (b) in presence of the PIM-EA-TB fragment leads to adsorbed  $\text{CO}_2^* + \text{H}^*$  (d) upon overcoming an energy barrier of 0.42 eV ( $E_R = -0.65$  eV). The same b species may dissociate to  $\text{HCO}^* + \text{O}^*$  (e), although a higher energy barrier and endothermic character make this process unlikely; further dehydrogenation of e would lead  $\text{CO}^*$ . Similarly,  $\text{COOH}^*$  (c) is more likely to decompose into d rather than on  $\text{CO}^* + \text{OH}^*$  (f), which, although slightly more exothermic than the former by 0.10 eV, has a formation energy barrier of 0.88 eV, then kinetically inhibiting  $\text{CO}^*$  formation.

On the naked Pd(111) surface, the decomposition of  $\text{HCOO}^*$  (b) and  $\text{COOH}^*$  (c) follow the same pathways than those on PIM-EA-TB fragment/Pd(111). Formate (b) leads to  $\text{CO}_2^* + \text{H}^*$  (d) because

$\text{HCO}^* + \text{O}^*$  (e) is energetically unfavourable. However, exothermic  $\text{CO}^*$  formation from c competes with d, which has a slightly endothermic formation energy but an activation barrier of only 0.10 eV (lower than that for f). The energy differences in the PIM-EA-TB presence and absence are clearly expressed by the energy profiles in Fig. 10A and 10B. Although the difference in overall activation energy is relatively small (0.15 eV), the most likely reaction pathway in the presence of PIM-EA-TB appears to be O–H dehydrogenation followed by C–H dehydrogenation.

The adsorbed CO on Pd(111) is well-known to poison the catalysts surface leading to its deactivation. However, there is no activity depletion observed in the experiments performed here with palladium embedded into microporous PIM-EA-TB. The simulation results imply that the role of the microstructure surrounding Pd nanoparticles not only facilitates the formic acid decomposition to  $\text{H}_2$  and  $\text{CO}_2$ , but it might also be promoting the mechanism leading to  $\text{CO}_2$  (Pathway 1) and suppressing formation of CO (Pathway 2), thereby preserving the Pd catalytic activity from declining due to CO poisoning.

### 3.4. Pd@PIM-EA-TB reactivity IV.: TMB oxidation in the presence of perchlorate

Having investigated Processes I and II individually (see Fig. 6C), it is now possible to re-examine the TMB colour reaction driven by  $\text{H}_2\text{O}_2$  production. Fig. 11 shows data for the reaction of TMB with



**Fig. 13.** Effects of Nafion ionomer printed on a filter paper on the TMB colour response with/without 50 mM  $\text{ClO}_4^-$  for 10 mM  $\text{HCOOH}/\text{HCOONa}$  concentration at pH 3.75. Photographs of 580  $\mu\text{M}$  TMB (A) without catalyst, (B) without Nafion, (C) in the absence of  $\text{ClO}_4^-$ , and (D) with  $\text{ClO}_4^-$  (stirred in the dark, 33 % DMSO, 11  $\text{cm}^3$ ) as a function of reaction time.

$\text{H}_2\text{O}_2$ , but without Pd@PIM-EA-TB catalyst- $\text{H}_2\text{O}_2$  is added at a level to mimic the catalytic reaction and the formation of the blue colour is observed clearly at 10 mM formate/formic acid pH 3.75 and higher. The same reaction in the presence of Pd@PIM-EA-TB and absence of added  $\text{H}_2\text{O}_2$  produces a similar pattern of colour starting at 10 mM, but a marked loss of TMB oxidation takes place at 50 mM and 100 mM formate/formic acid. The production of  $\text{H}_2\text{O}_2$  is unlikely to cease under these conditions, but the presence of hydrogen and possibly trace Pd(II) in the solution phase could adversely affect the TMB colour reaction at higher formate/formic acid concentration.

Next, the TMB colour reaction is investigated with Pd@PIM-EA-TB as a function of pH for 50 mM formate/formic acid. Fig. 12 shows the formation of a blue-green product (a mixture of blue mono- and yellow di-oxidised TMB) in the range from pH 2.5 to 3.5. At less acidic pH the production of  $\text{H}_2\text{O}_2$  is less effective and the colour is not produced. In the presence of perchlorate, a very similar pattern of reactivity is observed except that the blue colour is clear, and a blue precipitate is formed likely to be the blue TMB dimer (possibly protonated) as a perchlorate containing salt.

Although perchlorate is likely to produce higher concentration of  $\text{H}_2\text{O}_2$ , the effect on the colour reaction is not dramatic. Similar levels of coloration are observed in the presence (Fig. 12A) and in the absence (Fig. 12B) of perchlorate. However, the colour appears

to be deeper blue in the presence of perchlorate compared to more green as observed in the absence of perchlorate. Importantly, the colour reaction is different due to precipitation of the blue product in the presence of perchlorate. A precipitation or accumulation of the blue colour can be very useful for reproducibility and sensor effective read-out. Therefore, the optimised colour response with accumulation of the blue product into an indicator strip is investigated next.

### 3.5. Pd@PIM-EA-TB reactivity V.: optimized TMB colour reaction

The precipitation of a blue product due to TMB oxidation in the presence of perchlorate anions strongly suggests a cationic blue product (compare mechanism in Fig. 4A). In order to collect this blue cationic product and to produce a stronger colour change, Nafion ionomer can be employed. Here, we use Nafion ionomer printed with a stamp (see Fig. 13) onto filter paper.

Under optimised conditions (10 mM  $\text{HCOOH}/\text{HCOONa}$ , pH 3.75), a blue coloration slowly emerges due to Pd@PIM-EA-TB producing  $\text{H}_2\text{O}_2$ . A weak coloration is observed also without catalyst possibly due to slow aerial background TMB oxidation. In the presence of Pd@PIM-EA-TB, a much more obvious colour reaction is observed when employing a Nafion ionomer-printed filter paper. A beneficial effect of perchlorate is seen at 4 h and 5 h but, for more

prolonged reaction times, a clear colour response is seen also without addition of perchlorate. These experiments confirm the catalytic production of  $\text{H}_2\text{O}_2$  leading to TMB oxidation and colour response. A higher formate/formic acid concentration can be employed to speed up the process. Nafion ionomer printed onto filter paper has been shown to give clear colour contrast due to accumulation of the cationic blue colour product.

#### 4. Conclusions

It has been shown that palladium nanoparticles embedded into PIM-EA-TB exhibit nanozyme-like formate oxidase reactivity with production of hydrogen peroxide in the presence of aqueous formic acid. Molecular rigidity of the PIM-EA-TB host creates “cavities” at the surface of the palladium nanoparticles with a reactivity that is linked to the presence of the tertiary amine and the vicinity of the palladium surface. Although a range of populations of cavities will exist depending on palladium nanoparticle surface morphology and interaction to the PIM-EA-TB polymer, it can be proposed that similar effects to those illustrated in the DFT model study are likely to exist in similar configurations. Only one specific case was studied as a model system for the catalyst cavity effect. Further key results of this study are:

- Formic acid is reacting catalytically to give hydrogen peroxide in the presence of oxygen (formate oxidase reactivity).
- The interaction of PIM-EA-TB with the palladium nanoparticle surface creates a significant number of active catalytic sites.
- The solution pH triggers enhanced formation of  $\text{H}_2\text{O}_2$  at pH < 4 linked to the protonation of tertiary amines in PIM-EA-TB.
- Hydrogen formation in competition to hydrogen peroxide production is significant close to pH 4 but less important at more acidic or more alkaline conditions.
- Perchlorate affects the reaction at the palladium surface (providing more ammonium sites) and thereby enhances the production of  $\text{H}_2\text{O}_2$  in acidic solutions.
- A DFT analysis of possible reaction pathways in a model “cavity” formed by PIM-EA-TB at the palladium surface confirms that both oxygen hydrogenation and formic acid dehydrogenation are enhanced due to a lower activation barrier for both in the presence of the tertiary amine close to the palladium surface.
- The blue colour reaction of TMB with  $\text{H}_2\text{O}_2$  occurs in homogeneous solution and can be employed to follow  $\text{H}_2\text{O}_2$  production visually.
- Nafion ionomer can be employed to enhance the TMB colour reaction due to accumulation of the cationic blue species (at pH 3.75) into the anionic ionomer.

The effects of molecularly rigid intrinsically microporous polymers (PIMs) on catalytic and surface reactions remain intriguing and potentially open up a new methodology for catalyst development. In the future, PIMs can be designed to generate surface cavities to make catalysts more effective and more selective. DFT computational tools can provide powerful complementary information and may in the future be powerful predictors for catalytic reactivity and for optimised PIM molecular structures for catalysis at various types electrode/catalyst surfaces and for a variety of molecularly rigid PIM materials.

#### Data availability

Data will be made available on request.

#### Declaration of Competing Interest

The authors declare that they have no known competing financial interests or personal relationships that could have appeared to influence the work reported in this paper.

#### Acknowledgement

L.W. thanks the China Scholarship Council (201906870022) for a PhD stipend. F.M. thanks EPSRC for support under project EP/K004956/1. We also acknowledge Supercomputing Wales for access to the Hawk HPC facility, part-funded by the European Regional Development Fund via the Welsh Government.

#### Appendix A. Supplementary material

Supplementary data to this article can be found online at <https://doi.org/10.1016/j.jcat.2022.11.015>.

#### References

- [1] H.H. Rao, J.Y. Li, M.Y. Luo, K.H. Zhang, H. Gou, H.X. Liu, Z.H. Xue, Nanozyme electroanalysis A label-free and modification-free ratiometric electrochemical strategy for enhanced natural enzyme detection using a bare electrode and nanozymes system, *Anal. Bioanal. Chem.* 414 (9) (2022) 2991–3003.
- [2] K. Bialas, D. Moschou, F. Marken, P. Estrela, Electrochemical sensors based on metal nanoparticles with biocatalytic activity, *Microchim. Acta* 189 (4) (2022) 172.
- [3] N. Stasyuk, O. Smutok, O. Demkiv, T. Prokopiv, G. Gayda, M. Nisnevitch, M. Gonchar, Synthesis, catalytic properties and application in biosensing of nanozymes and electronanocatalysts: a review, *Sensors* 20 (16) (2020) 4509.
- [4] F. Tieves, S.J.P. Willot, M.M.C.H. Schie, M.C.R. Rauch, S.H.H. Younes, W.Y. Zhang, J.J. Dong, P.G. Santos, J.M. Robbins, B. Bommarius, M. Alcalde, A.S. Bommarius, F. Hollmann, Formate Oxidase (FOx) from *Aspergillus oryzae*: one catalyst enables diverse  $\text{H}_2\text{O}_2$ -dependent biocatalytic oxidation reactions, *Angew. Chem. Int. Ed.* 58 (2019) 7873–7877.
- [5] L.Z. Gao, X.Y. Yan, Discovery and current application of nanozyme, *Prog. Biochem. Biophys.* 40 (10) (2013) 892–902.
- [6] H.L. Wapshott-Stehli, A.M. Grunden, In situ  $\text{H}_2\text{O}_2$  generation methods in the context of enzyme biocatalysis, *Enzyme Microbial Technol.* 145 (2021).
- [7] Q.Q. Wang, H. Wei, Z.Q. Zhang, E.K. Wang, S.J. Dong, Nanozyme: An emerging alternative to natural enzyme for biosensing and immunoassay, *TRAC - Trends Anal. Chem.* 105 (2018) 218–224.
- [8] J.M. Robbins, J.F. Geng, B.A. Barry, G. Gadda, A.S. Bommarius, Photoirradiation generates an ultrastable 8-formyl FAD semiquinone radical with unusual properties in formate oxidase, *Biochem.* 57 (40) (2018) 5818–5826.
- [9] Y. Maeda, D. Doubayashi, M. Oki, H. Nose, A. Sakurai, K. Isa, Y. Fujii, H. Uchida, Expression in *Escherichia coli* of an unnamed protein gene from *Aspergillus oryzae* RIB40 and cofactor analyses of the gene product as formate oxidase, *Biosci. Biotechnol. Biochem.* 73 (12) (2009) 2645–2649.
- [10] V.O. Popov, V.S. Lamzin,  $\text{NAD}^+$ -dependent formate dehydrogenase, *Biochem. J.* 301 (3) (1994) 625–643.
- [11] A. Mehri, H. Kochkar, In situ generated  $\text{H}_2\text{O}_2$  over supported Pd-Au clusters in hybrid titania nanocrystallites, *Chem. Lett.* 43 (7) (2014) 1046–1048.
- [12] P.M. Budd, B.S. Ghanem, S. Makhseed, N.B. McKeown, K.J. Msayib, C.E. Tattershall, Polymers of intrinsic microporosity (PIMs): robust, solution-processable, organic nanoporous materials, *Chem. Commun.* 2 (2004) 230–231.
- [13] F. Marken, M. Carta, N.B. McKeown, Polymers of intrinsic microporosity in the design of electrochemical multicomponent and multiphase interfaces, *Anal. Chem.* 93 (3) (2021) 1213–1220.
- [14] E. Madrid, Y.Y. Rong, M. Carta, N.B. McKeown, R. Malpass-Evans, G.A. Attard, T. J. Clarke, S.H. Taylor, Y.T. Long, F. Marken, Metastable ionic diodes derived from an amine-based polymer of intrinsic microporosity, *Angew. Chem. Int. Ed.* 53 (40) (2014) 10751–10754.
- [15] S.D. Ahn, A. Kolodziej, R. Malpass-Evans, M. Carta, N.B. McKeown, S.D. Bull, A. Buchard, F. Marken, Polymer of intrinsic microporosity induces host-guest substrate selectivity in heterogeneous 4-benzoyloxy-TEMPO-catalysed alcohol oxidations, *Electrocatalysis* 7 (1) (2016) 70–78.
- [16] Y.Y. Rong, R. Malpass-Evans, M. Carta, N.B. McKeown, G.A. Attard, F. Marken, High density heterogenisation of molecular electrocatalysts in a rigid intrinsically microporous polymer, *Electrochem. Commun.* 46 (2014) 26–29.
- [17] D.P. He, Y.Y. Rong, M. Carta, R. Malpass-Evans, N.B. McKeown, F. Marken, Fuel cell anode catalyst performance can be stabilized with a molecularly rigid film of polymers of intrinsic microporosity (PIM), *RSC Adv.* 6 (11) (2016) 9315–9319.
- [18] Y.Z. Zhao, R. Malpass-Evans, M. Carta, N.B. McKeown, P.J. Fletcher, G. Kociok-Kohn, D. Lednitsky, F. Marken, Size-selective photoelectrochemical reactions in microporous environments: Clark probe investigation of  $\text{Pt@g-C}_3\text{N}_4$

- embedded into intrinsically microporous polymer (PIM-1), *ChemElectroChem* 8 (18) (2021) 3499–3505.
- [19] D.P. He, D.S. He, J.L. Yang, Z.X. Low, R. Malpass-Evans, M. Carta, N.B. McKeown, F. Marken, Molecularly rigid microporous polyamine captures and stabilizes conducting platinum nanoparticle networks, *ACS Appl. Mater. Interfaces* 8 (34) (2016) 22425–22430.
- [20] F.J. Xia, M. Pan, S.C. Mu, R. Malpass-Evans, M. Carta, N.B. McKeown, G.A. Attard, A. Brew, D.J. Morgan, F. Marken, F. Polymers of intrinsic microporosity in electrocatalysis: Novel pore rigidity effects and lamella palladium growth, *Electrochim. Acta* 128 (2014) 3–9.
- [21] L.N. Wang, M. Carta, R. Malpass-Evans, N.B. McKeown, P.J. Fletcher, D. Lednitsky, F. Marken, Hydrogen peroxide versus hydrogen generation at bipolar Pd/Au nano-catalysts grown into an intrinsically microporous polyamine (PIM-EA-TB), *Electrocatalysis* 12 (6) (2021) 771–784.
- [22] D. Liu, Z.Y. Gao, X.C. Wang, J. Zeng, Y.M. Li, DFT study of hydrogen production from formic acid decomposition on Pd-Au alloy nanoclusters, *Appl. Surf. Sci.* 426 (2017) 194–205.
- [23] M. Ab Rahim, M.M. Forde, C. Hammond, R.L. Jenkins, N. Dimitratos, J.A. Lopez-Sanchez, A.F. Carley, S.H. Taylor, D.J. Willock, G.J. Hutchings, Systematic study of the oxidation of methane using supported gold palladium nanoparticles under mild aqueous conditions, *Topics Catal.* 56 (18–20) (2013) 1843–1857.
- [24] H. Wang, K.W. Wan, X.H. Shi, Recent advances in nanozyme research, *Adv. Mater.* 31 (45) (2019) 1805368.
- [25] N. Stasyuk, O. Smutok, O. Demkiv, T. Prokopiv, G. Gayda, M. Nisnevitch, M. Gonchar, Nanozymes synthesis, catalytic properties and application in biosensors of nanozymes and electronanocatalysts: a review, *Sensors* 20 (16) (2020) 4509.
- [26] M.A. Komkova, K.R. Vetoshev, E.A. Andreev, A.A. Karyakin, Flow-electrochemical synthesis of Prussian Blue based nanozyme 'artificial peroxidase', *Dalton Trans.* 50 (33) (2021) 11385–11389.
- [27] B. Das, J.L. Franco, N. Logan, P. Balasubramanian, M.I. Kim, C. Cao, Nanozymes in point-of-care diagnosis: an emerging futuristic approach for biosensing, *Nano- Micro Lett.* 13 (1) (2021) 193.
- [28] L. Wu, S.H. Zhou, G.L. Wang, Y.H. Yun, G.Z. Liu, W.M. Zhang, Nanozyme applications: a glimpse of insight in food safety, *Frontiers Bioeng. Biotechnol.* 9 (2021).
- [29] X. Li, L. Wang, D. Du, L. Ni, J. Pan, X. Niu, Emerging applications of nanozymes in environmental analysis: Opportunities and trends, *TRAC - Trends Anal. Chem.* 120 (2019) 115653.
- [30] X.B. Xie, L. Tan, S.Y. Liu, X.Y. Wen, T. Li, M.H. Yang, High-sensitive photometric microplate assay for tumor necrosis factor- $\alpha$  based on Fe@BC nanozyme, *J. Immunol. Methods* 499 (2021).
- [31] A. Swaidan, A. Addad, J.F. Tahon, A. Barras, J. Toufaily, T. Hamieh, S. Szunerits, R. Boukherroub, Ultrasmall CuS-BSA-Cu<sub>3</sub>(PO<sub>4</sub>)<sub>2</sub> nanozyme for highly efficient colorimetric sensing of H<sub>2</sub>O<sub>2</sub> and glucose in contact lens care solutions and human serum, *Anal. Chim. Acta* 1109 (2020) 78–89.
- [32] F.J. Cui, Q.F. Deng, L. Sun, Prussian blue modified metal-organic framework MIL-101(Fe) with intrinsic peroxidase-like catalytic activity as a colorimetric biosensing platform, *RSC Adv.* 5 (119) (2015) 98215–98221.
- [33] N. Borah, C. Tamuly, Ultrasensitive Pd nano catalyst as peroxidase mimetics for colorimetric sensing and evaluation of antioxidants and total polyphenols in beverages and fruit juices, *Talanta* 238 (1) (2022).
- [34] M. Carta, R. Malpass-Evans, M. Croad, Y. Rogan, J.C. Jansen, P. Bernardo, F. Bazzarelli, N.B. McKeown, An efficient polymer molecular sieve for membrane gas separations, *Science* 339 (6117) (2013) 303–307.
- [35] L.I. Elding, Palladium(II) halide complexes. I. Stabilities and spectra of palladium(II) chloro and bromo aqua complexes, *Inorg. Chim. Acta* 6 (1972) 647–651.
- [36] G. Kresse, J. Furthmüller, Efficiency of ab-initio total energy calculations for metals and semiconductors using a plane-wave basis set, *Comp. Mater. Sci.* 6 (1) (1996) 15–50.
- [37] B. Hammer, L.B. Hansen, J.K. Nørskov, Improved adsorption energetics within density-functional theory using revised Perdew-Burke-Ernzerhof functionals, *Phys. Rev. B* 59 (11) (1999) 7413–7421.
- [38] P.E. Blöchl, Projector augmented-wave method, *Phys. Rev. B* 50 (24) (1994) 17953–17979.
- [39] S. Grimme, S. Ehrlich, L. Goerigk, Effect of the damping function in dispersion corrected density functional theory, *J. Comp. Chem.* 32 (7) (2011) 1456–1465.
- [40] K. Mathew, V.S. Chaitanya Kolluru, S. Mula, S.N. Steinmann, R.G. Hennig, Implicit self-consistent electrolyte model in plane-wave density-functional theory, *J. Chem. Phys.* 151 (2019).
- [41] K. Mathew, R. Sundaraman, K. Letchworth-Weaver, T.A. Arias, R.G. Hennig, Implicit solvation model for density-functional study of nanocrystal surfaces and reaction pathways, *J. Chem. Phys.* 140 (2014).
- [42] G. Henkelman, H. Jónsson, Improved tangent estimate in the nudged elastic band method for finding minimum energy paths and saddle points, *J. Chem. Phys.* 113 (2000) 9978.
- [43] G. Henkelman, A climbing image nudged elastic band method for finding saddle points and minimum energy paths, *J. Chem. Phys.* 113 (2000) 9901.
- [44] G. Henkelman, H. Jónsson, A dimer method for finding saddle points on high dimensional potential surfaces using only first derivatives, *J. Chem. Phys.* 111 (1999) 7010.
- [45] D.M. Liu, B.J. Xu, C. Dong, Recent advances in colorimetric strategies for acetylcholinesterase assay and their applications, *TRAC Trends Anal. Chem.* 142 (2021).
- [46] P.D. Josephy, T. Eling, R.P. Mason, The horseradish peroxidase-catalyzed oxidation of 3,5,3',5'-tetramethylbenzidine - free-radical and charge-transfer complex intermediates, *J. Biol. Chem.* 257 (7) (1982) 3669–3675.
- [47] X. Zhang, Q. Yang, Y.H. Lang, X. Jiang, P. Wu, Rationale of 3,3',5,5'-tetramethylbenzidine as the chromogenic substrate in colorimetric analysis, *Anal. Chem.* 92 (18) (2020) 12400–12406.
- [48] S.J. Zhuo, J. Fang, C.Q. Zhu, J.Y. Du, Preparation of palladium/carbon dot composites as efficient peroxidase mimics for H<sub>2</sub>O<sub>2</sub> and glucose assay, *Anal. Bioanal. Chem.* 412 (4) (2020) 963–972.
- [49] J.S. Mu, Y. Wang, M. Zhao, L. Zhang, Intrinsic peroxidase-like activity and catalase-like activity of Co<sub>3</sub>O<sub>4</sub> nanoparticles, *Chem. Commun.* 48 (19) (2012) 2540–2542.
- [50] L. Kham, Y. Le Bigot, M. Delmas, G. Avignon, Delignification of wheat straw using a mixture of carboxylic acids and peroxyacids, *Ind. Crops Products* 21 (1) (2005) 9–15.
- [51] Z.S. Petrovic, A. Zlatanic, C.C. Lava, S. Sinadinovic-Fiser, Epoxidation of soybean oil in toluene with peroxyacetic and peroxyformic acids - kinetics and side reactions, *Europ. J. Lipid Sci. Technol.* 104 (5) (2002) 293–299.
- [52] I. Elkin, P. Hildgen, Selective synthesis of glyceryl tris[9,10-(threo)-dihydroxy-octadecanoate], *J. Amer. Oil Chem. Soc.* 90 (10) (2013) 1465–1474.
- [53] D. Swern, Epoxidation and hydroxylation of ethylenic compounds with organic peracids. In: *Organic reactions* (Online). 2004, Wiley, doi:10.1002/0471264180.or007.07.
- [54] D. Swern, G.N. Billen, T.W. Findley, J.T. Scanlan, Hydroxylation of monounsaturated fatty materials with hydrogen peroxide, *J. Am. Chem. Soc.* 67 (1945) 1786–1789.
- [55] Y.Y. Rong, A. Kolodziej, E. Madrid, M. Carta, R. Malpass-Evans, N.B. McKeown, F. Marken, Polymers of intrinsic microporosity in electrochemistry: Anion uptake and transport effects in thin film electrodes and in free-standing ionic diode membranes, *J. Electroanal. Chem.* 779 (2016) 241–249.
- [56] T. Shimaouchi, Tables of Molecular Vibrational Frequencies Consolidated, Volume 1, National Bureau of Standards, Washington D.C., 1972, NBS NSRDS 39.
- [57] R.L. Redington, W.B. Olson, P.C. Cross, Studies of hydrogen peroxide: the infrared spectrum and the internal rotation problem, *J. Chem. Phys.* 36 (1962) 1311.
- [58] D.C. Ford, A.U. Nilekar, Y. Xu, M. Mavrikakis, Partial and complete reduction of O<sub>2</sub> by hydrogen on transition metal surfaces, *Surf. Sci.* 604 (19–20) (2010) 1565–1575.
- [59] F. Sanchez, M. Hayal Alotaibi, D. Motta, C.E. Chan-Thaw, A. Rakotomahevitra, T. Tabanelli, A. Roldan, C. Hammond, Q. He, T. Davies, A. Villa, N. Dimitratos, Hydrogen production from formic acid decomposition in the liquid phase using Pd nanoparticles supported on CNFs with different surface properties, *Sust. Energy Fuels* 2 (2018) 2705–2716.
- [60] F. Sanchez, D. Motta, A. Roldan, C. Hammond, A. Villa, N. Dimitratos, Hydrogen generation from additive-free formic acid decomposition under mild conditions by Pd/C: experimental and DFT studies, *Topics Catal.* 61 (2018) 254–266.
- [61] I. Barlocco, S. Bellomi, J.J. Delgado, X.W. Chen, L. Prati, N. Dimitratos, A. Roldan, A. Villa, Enhancing activity, selectivity and stability of palladium catalysts in formic acid decomposition: effect of support functionalization, *Catal. Today* 382 (2021) 61–70.
- [62] I. Barlocco, S. Capelli, X.Y. Lu, S. Bellomi, X.H. Huang, D. Wang, L. Prati, N. Dimitratos, A. Roldan, A. Villa, Disclosing the role of gold on palladium - gold alloyed supported catalysts in formic acid decomposition, *ChemCatChem* 13 (19) (2021) 4210–4222.